

MoSAIC: Multi-Resolution Spatial Regression Analysis of Cellular Colocalizations in Cancer Imaging

Jessica Aldous¹, Michele Peruzzi¹, Maria Masotti², Aaron Udager³, Allison May⁴, Evan Keller⁵, and Veerabhadran Baladandayuthapani¹

¹Department of Biostatistics, University of Michigan

² Hennepin Healthcare Research Institute

³Department of Pathology, University of Michigan

⁴Department of Urology, University of Virginia

⁵Department of Urology, University of Michigan

May 29, 2026

Abstract

Hierarchical multiplex imaging approaches generate spatially resolved single-cell measurements across multiple, spatially organized fields of view (FOVs) within patient tumor specimens, thereby enabling systematic investigation of how the organization of the tumor microenvironment varies along biologically meaningful intratumoral gradients. Existing approaches fail to jointly address this multi-resolution data structure needed to recover true biological signals. We propose **MoSAIC**: *multi-resolution spatial regression analysis of cell colocalizations*, a hierarchical Bayesian spatial regression model designed for multi-resolution spatial data. **MoSAIC** decomposes the joint variation into three model components: (i) global tumor-gradient effects, (ii) patient-specific effects to capture inter-patient variability, and (iii) Gaussian process models to account for spatial dependence between FOVs within each patient tumor tissue. Simulations demonstrate **MoSAIC** has improved prediction and model fit compared to existing spatial and non-spatial model alternatives. Our method is motivated by and applied to a renal cell carcinoma multiplex imaging cohort to investigate immune-tumor colocalization patterns across the epithelial-to-mesenchymal transition (EMT) gradient. **MoSAIC** identifies increased macrophage-tumor colocalization and decreased cytotoxic T-tumor colocalization progressing across the increasing EMT gradient, consistent with EMT-associated immune suppression and spatially varying immune engagement. Overall, **MoSAIC** provides an interpretable, multi-resolution framework for quantifying spatial tumor-gradient effects in cancer imaging studies. Software is available on Github at [jcaldous/MoSAIC](https://github.com/jcaldous/MoSAIC).

Keywords: Gaussian Processes, Hierarchical Bayes, Multiplex Imaging, Renal Cell Carcinoma, Spatial Regression

1 Introduction

Influence of tumor microenvironment in cancer. As cancer develops, tumor cells alter their environment to support survival and progression (Hinshaw & Shevde 2019). This interplay between tumor cells, immune cells and the surrounding stroma forms a complex tumor ecosystem, termed the tumor microenvironment (TME; Boyk et al. 2022). Evidence suggests spatial positions of immune cells within the TME can influence drug resistance (van Dam et al. 2022) and either promote or suppress tumorigenesis (Anderson & Simon 2020). For example, a high infiltration of M2 macrophages, white blood cells involved in wound healing, can promote tumor growth and is associated with poorer patient prognosis (Tripathi et al. 2014). In contrast, cytotoxic T cells target tumor cells by identifying abnormal antigens and an abundance of this immune cells is generally associated with better prognosis (Anderson & Simon 2020). Recent developments in spatial multiplex imaging technologies, such as tissue-based cyclic immunofluorescence (Lin et al. 2018) and multiplexed ion beam imaging (Ptacek et al. 2020), have enabled a more systematic and quantitative investigation of the TME (Lewis et al. 2021). These technologies generate rich datasets with measures of phenotypic and functional protein markers at the cellular level while maintaining the spatial relationships between cells within the tumor.

Sarcomatoid renal cell carcinoma. In the context of kidney cancers, particularly renal cell carcinoma (RCC), studies have delineated the critical role of the TME and its components in RCC biology and progression (Heidegger et al. 2019). Of particular interest is the involvement of the TME in initiating the epithelial to mesenchymal transition (EMT), a biological process that causes epithelial cells to progressively lose their typical features for a mesenchymal-like phenotype, marking significant changes in cell invasiveness (He & Magi-Galluzzi 2014). The EMT is associated with sarcomatoid dedifferentiation in RCC (sRCC), an aggressive form of renal cancer (Blum et al. 2020). Importantly, sRCC is not a unique

histological subtype but rather a cell dedifferentiation that can occur anywhere in the tumor. Thus, one tumor contains cells at various stages along the EMT gradient. Although the EMT is a well-described oncogenic pathway, the role of the microenvironment in initiating this transition to more aggressive disease remains poorly understood in RCC. Recent studies also revealed that sRCC is increasingly sensitive to immunotherapy compared to clear cell RCC, suggesting that immune-tumor cell colocalization may differ across the EMT gradient (Tripathi et al. 2014). Consequently, our primary scientific question focuses on how cellular colocalizations vary *across* the tumor gradient both within and across patient tumors.

Tumor gradients and hierarchical multiplex imaging data. Spatial multiplex imaging data offers an ideal platform for scientific investigations of the tumor gradient, as it measures both spatial biomarker expression and cellular spatial relationships. Since tumor tissues are large and heterogeneous, studies often focus on sampling smaller subsections of the tumors, called fields of view (FOVs). These spatially resolved replicates enable the study of the TME both within and across patients in a cost-effective manner, resulting in a hierarchical data structure that we call Hierarchical Multiplex Imaging (HMI). The general structure of HMI data from our sRCC data is presented in Figure 1. Each patient (A) has a tumor tissue scan with spatially organized FOVs sampled across the two-dimensional tumor tissue space (B). Each FOVs has a corresponding spatial distribution of the cells (C), wherein each shape and color represents a unique cell type. FOVs are colored by a continuous biomarker that tracks the EMT across the tumor tissue (D). Our scientific focus is on quantifying changes in cellular organization across this EMT gradient.

Existing methods and limitations. This HMI data structure presents several unique analytical challenges. Specifically, (a) the complex spatial relationships among cells in a single FOV; (b) the non-ignorable spatial dependency between FOVs of a single tumor tissue; and (c) the high degree of both within- and between-patient variability (heterogeneity), which must all be considered to quantify true biological gradient within and across

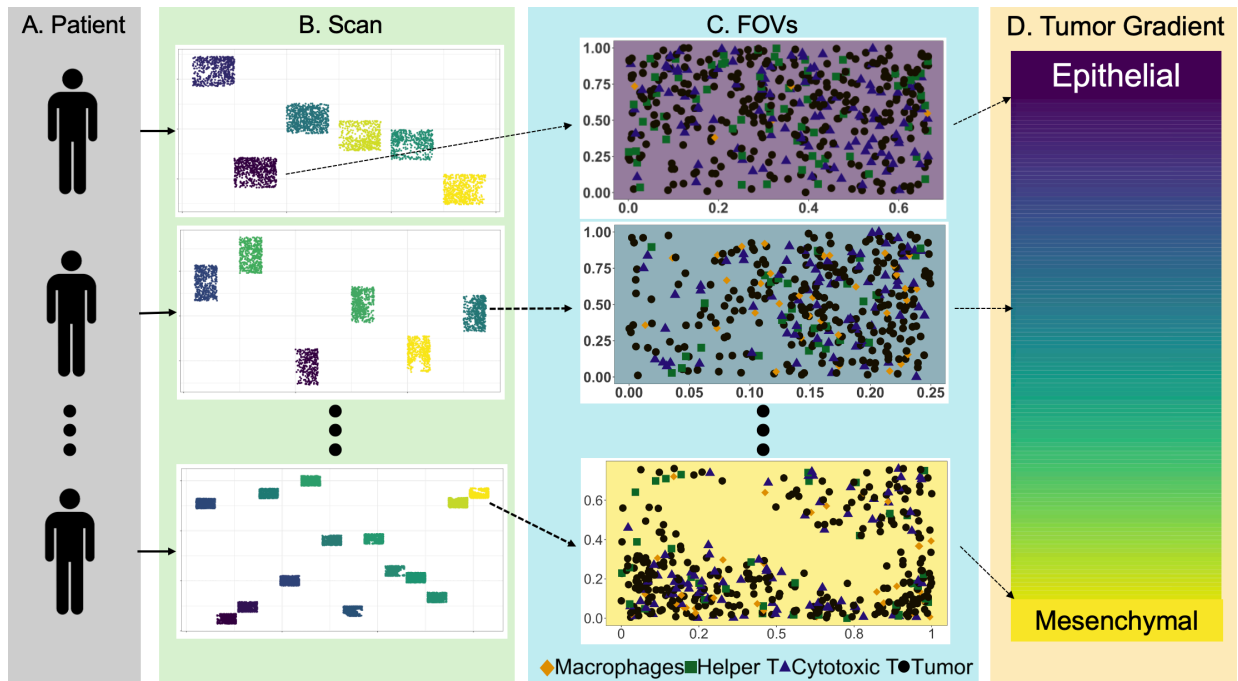


Figure 1: **Hierarchical multiplex imaging data structure in sRCC.** Each patient (A) has a tumor tissue scan with multiple FOVs (B). Each FOV (C) is composed of 4 different cell types (macrophages: orange diamonds, helper T: green squares, cytotoxic T: navy triangles, Tumor: black circles). FOVs are colored based on a continuous biomarker (D) of the EMT gradient (purple: clear cell; yellow: sarcomatoid).

the patient tumor tissues. Existing methods for addressing some of these challenges can be broadly split into two categories: summary-based and model-based. Several summary-based methods have been proposed (Wrobel et al. 2023), and they typically quantify cellular colocalizations within each image (FOV) that can be utilized in downstream cross-patient analyses (Mohammed et al. 2024). Examples include cross functions like Ripley’s K-cross (Ripley 1976) and G-cross (Baddeley et al. 2016), density-based methods like DIMPLE (Masotti et al. 2023), and others like MIAMI (Seal & Ghosh 2022) which models the phenotypic expression directly as opposed to the discrete cell types. These summary-based models are well-suited for characterizing immune-tumor cellular colocalizations within a *single* sample/FOV but ignore (spatial) relationships between FOVs. As a result, they are

not readily scalable or adaptable to the hierarchical dependence structures of HMI data.

Existing model-based methods are limited in their ability to account for every source of variability. Standard mixed effects regression models (Galecki & Burzykowski 2013) can borrow strength across patient data, but they ignore spatial dependencies among FOVs, which can lead to artificially low p-values and inflated effect sizes (Shaked 1980, Lennon 2000). Neighborhood-based methods such as conditional autoregressive (CAR) models (Besag et al. 1991) are poorly suited for HMI since tumor tissues are non-conformable spaces; patient tumors have different shapes, EMT gradients, and numbers of FOVs leading to very different neighborhoods (Banerjee et al. 2015). Gaussian Processes (GP; Rasmussen & Williams 2005) offer a more flexible alternative to capture the spatial relationships between FOVs, but currently available GP models for cellular colocalization were not developed to accommodate spatially resolved within-patient replicates, making them difficult to implement (Arnol et al. 2019). Few models (e.g. Seal et al. 2024; Canete et al. 2022; Eliason & Rao 2024; Eliason et al. 2025; Kondo et al. 2021) borrow information across patients with multiple images to investigate differences in cell colocalization across patient cohorts. However, none of these methods account for a hierarchical relationship within and between images, and their simplifying assumptions make their direct application unsuitable for HMI data.

Multi-resolution spatial regression analysis of cell colocalizations in cancer.

To this end, we propose MoSAIC: multi-resolution spatial regression analysis of cell colocalizations. MoSAIC seeks to bridge the gap between these approaches, culminating in a procedure that disentangles the layers of within- and between-patient variability to produce interpretable estimates. Specifically, we employ a hierarchical Bayesian spatial regression model that quantifies the effect of the tumor gradient on the TME while accounting for the spatial relationship between the FOVs and the between-patient heterogeneity. We model

the tumor gradient nonlinearly using spline-based basis functions and incorporate GP-based random effects to capture spatial dependencies among FOVs. The resulting model produces interpretable coefficient curves that highlight how cellular colocalizations change across the tumor gradient and appropriately accommodate between-patient variability. In multiple simulation settings, MoSAIC demonstrates improved predictive performance and model fit compared to spatial and non-spatial model alternatives for HMI data. When applied to sRCC HMI data, MoSAIC detects alterations in the spatial colocalization patterns of immune cells—specifically cytotoxic T cells and macrophages—with tumor cells along the EMT gradient.

Our paper is organized as follows. Section 2 details the MoSAIC model, including model construction, estimation, and posterior inference. Section 3 outlines the comparative simulation studies, followed by Section 4 that applies MoSAIC to the sRCC HMI data. Section 5 ends with some concluding thoughts and a discussion on model extensions and generalizations. Supplemental material covers additional modeling details, simulation results, and figures. Software for fitting MoSAIC is freely available on Github at [jcaldous/MoSAIC](https://github.com/jcaldous/MoSAIC).

2 MoSAIC Model

HMI data structure and notations. We denote each patient by $i = 1, \dots, I$ and their tumor tissue space by \mathcal{D}_i . Within each \mathcal{D}_i , we sample a set of n_i non-overlapping FOVs indexed by $j(i) = 1, \dots, n_i$. We represent each FOV by their centroid locations, $s_{j(i)}$, which denote the patient subspace $\mathcal{S}_i \subset \mathcal{D}_i$. In our setting, we have two hierarchical spatial resolutions in our sRCC HMI data: (a) a fine-scale resolution consisting of cells, which are nested within (b) a coarser-scale resolution of FOVs sampled across a given tumor tissue for a given patient. We develop MoSAIC to leverage the FOV level information to investigate the influence of the tumor gradient across the entire tumor tissue. Our patient subspace

\mathcal{S}_i is comprised of FOVs sampled across the patient tumor tissue \mathcal{D}_i but MoSAIC can be applied to any data set with spatial locations across many replicates (e.g. cells within an FOV).

For a given patient subspace \mathcal{S}_i , let $y(s_{j(i)})$ be our outcome measured at $s_{j(i)}$. We denote our p covariates measured at $s_{j(i)}$ as $x(s_{j(i)}) = \{x_1(s_{j(i)}), \dots, x_p(s_{j(i)})\}$. In our RCC data, $y(s_{j(i)})$ is a scalar quantifying the degree of immune-tumor cellular interactions for an FOV with centroid $s_{j(i)}$, and $x(s_{j(i)})$ denotes a vector storing the expression level of p biomarkers within an FOV representative of the tumor gradient. To better estimate complex global (population level) relationships between $x(s_{j(i)})$ and $y(s_{j(i)})$, we borrow strength across the patient cohort while accounting for within patient (spatial) heterogeneity. To this end, we estimate the effect of the $x(s_{j(i)})$ on $y(s_{j(i)})$ as follows:

$$y(s_{j(i)}) = g(x(s_{j(i)})) + \mu_i + \psi(s_{j(i)}) + \epsilon_{j(i)},$$

where $g(x(s_{j(i)}))$ is the global covariate effect capturing the tumor gradient, μ_i is the patient-specific intercept, $\psi(s_{j(i)})$ is the spatial random effect, and $\epsilon_{j(i)}$ captures the residual measurement error.

Aggregating data across all I patients, let $y_{N \times 1} = [y^T(\mathcal{S}_1), \dots, y^T(\mathcal{S}_I)]^T$ denote the concatenated vector of outcomes. For ease of exposition, we represent the covariates of interest across all I patients by matrix $X_{N \times p}$ and the block-diagonal design matrix that maps the vector of patient-specific intercepts ($\mu_{I \times 1}$) to the N total observation by $Z_{N \times I}$. We also vectorize the spatial random effects ($\psi_{N \times 1}$) and measurement errors ($\epsilon_{N \times 1}$). The resulting population level MoSAIC model is as follows:

$$y = g(X) + Z\mu + \psi + \epsilon, \quad \text{and} \quad \psi \sim GP(0, \tau^2 C_\phi),$$

$$g(X) = B\theta = \sum_{l=1}^p B_l \theta_l = \sum_{l=1}^p \sum_{k=1}^{K_l} B_{kl} \theta_{kl}, \tag{1}$$

where B_{kl} is the k^{th} basis functions for a given set of K_l knots for the l^{th} covariate x_l , θ_{kl}

is the corresponding basis coefficient, and the spatial random effect ψ follows a Gaussian Process with covariance kernel C_ϕ .

Covariate effects. We decompose our covariate effects in equation (1) into global effects ($g(X)$) and patient-specific intercepts ($Z\mu$). Patient specific intercepts, μ , allow us to account for the variability between patients that can obscure the global impact of X across patients. The associations between the X and y across all patients may be complex and require a flexible solution to estimate. MoSAIC accommodates possible non-linear associations and smooths across patients by specifying spline-based basis functions (De Boor 1978, Dierckx 1993). Specifically, we use penalized splines as specified by Eilers & Marx (1996); relevant alternatives include Bayesian penalized splines (Crainiceanu et al. 2005) and low-rank predictive processes (Huang & Sun 2018). Thus, we estimate a single set of coefficients θ across patients and individualize tumor gradients for each patient through B .

We assign a normal prior to the patient intercepts, $\mu \sim N(0, \sigma_Z^2 I_I)$, and covariate estimates, $\theta_l \sim N(0, \sigma_l^2 K)$, for all $l = 1, \dots, p$. K is a positive-definite matrix, and we set $K = I$ when $g(x_l)$ is linear and $K = D^T D$ when $g(x_l)$ is non-linear. The penalty matrix D is the second-order difference operator matrix that shrinks the difference between neighboring basis coefficients, leading to smoothed estimation of the covariate effects (Eilers & Marx 1996). The hyperparameters $\{\sigma_1^2, \dots, \sigma_p^2\}$ control the amount of shrinkage on $\theta = \{\theta_1^T, \dots, \theta_p^T\}^T$ (towards 0), further enabling smoothing as well as controlling overfitting. If we standardize our covariates to be on a similar scale, we can apply the same σ_X^2 for all p covariates. For linear terms, σ_l^2 is set to a large value (minimal shrinkage); otherwise, we apply an inverse-gamma priors to both variance terms $\sigma_X^2 \sim IG(a_x, b_x)$ and $\sigma_Z^2 \sim IG(a_z, b_z)$, allowing adaptive shrinkage.

Spatial random effects. The spatial random effect, ψ , captures the spatial relationship between FOVs within a given tumor tissue, \mathcal{S}_i . We expect FOVs in close spatial proximity

to be more similar than those that are more distant within a given tumor tissue. Thus, our GP assumption on ψ yields $\psi \sim N(0, \tau^2 C_\phi)$, where C_ϕ is the kernel matrix. In our RCC setting, C_ϕ specifies the correlation between two FOVs as a function of their distance and the spatial decay term, ϕ . The spatial decay ϕ controls the degree of spatial smoothing between FOVs with large ϕ values limiting smoothing to FOVs very near one another. Importantly, we only want to smooth among locations *within the same patient* since observations from two different patients do not have a scientifically meaningful spatial relationship. Therefore, we specify the elements of C_ϕ via a squared exponential kernel such that there is independence across patients:

$$C_\phi(s_i, s_{i'}) = \exp\{-\phi\|s_i - s_{i'}\|^2\} \mathbb{1}(i = i').$$

The parameter τ^2 captures the spatial variance magnitude. We borrow information across patients to estimate common τ^2 and ϕ since we expect there to be a similar spatial structure across patients. We posit a non-informative inverse-gamma prior on τ^2 , such that $\tau^2 \sim IG(a_s, b_s)$. We fix the spatial decay hyperparameter, ϕ , from a series of values through a test-training procedure (details in Supplement S1).

Measurement error. The measurement error term ϵ captures any remaining variability in the outcome not explained by the covariate gradient, spatial relationship between observations, or patient differences. We specify $\epsilon \sim N(0, \sigma_y^2 I_N)$ and $\sigma_y^2 \sim IG(a_y, b_y)$.

2.1 Posterior estimation and inference

Posterior sampling. Since we posit Gaussian priors to θ, ψ, μ and ϵ , we can sample from the marginal model,

$$y \sim N(0, \Sigma_y); \quad \Sigma_y = \sigma_X^2 \sum_{l=1}^p B_l K B_l^T + \sigma_Z^2 Z Z^T + \tau^2 C_\phi + \sigma_y^2 I_N, \quad (2)$$

with 4 free parameters: $\sigma_Z^2, \sigma_X^2, \tau^2, \sigma_y^2$. Marginalized parameters (θ, μ, ψ) are recovered from the joint posterior. This formulation improves convergence and mitigates identifiability

ity concerns between μ and ψ . To fit MoSAIC, we implement a robust adaptive Metropolis algorithm as specified by Vihola (2012) to sample the variance terms, $\{\sigma_Z^2, \sigma_X^2, \tau^2, \sigma_y^2\}$, from equation 2 (details in Supplement S1). By implementing an adaptive algorithm that updates the proposal distribution to shrink or expand towards the desired acceptance probability, MoSAIC explores the posterior more efficiently. We calculate the Deviance Information Criteria (DIC; Spiegelhalter et al. 2002) and scaled Watanabe–Akaike Information Criterion (WAIC; Watanabe & Opper 2010), which use log predictive density penalized by the number of effective parameters to derive Bayesian measures of model fit (Gelman et al. 2014).

Joint credible bands and global significance. In addition to estimating the global covariate effects $g(X)$, we are interested in quantifying the amount of uncertainty around those estimates and testing for significance. While point-wise credible bands suffice for linear coefficients, there is an inherent multiple testing issue when inferring smoothed covariate functions since we are generating estimates over a continuum of values X (Ruppert et al. 2009). To address this, we use joint credible bands similar to those proposed by Meyer et al. (2015). Briefly, we estimate $100(1 - \alpha)^{th}$ joint-credible bands such that the probability of $g(X)$ being in that interval is greater than or equal to $1 - \alpha$ for *all values* of X , thus naturally allowing for multiple testing correction. This strategy also enables assessment of a global Bayesian p-value to test the null hypothesis that the relationship between our tumor gradient and the outcome is significantly different from 0 across the entire tumor gradient (further details in Supplement Section S1).

Variance decomposition. The construction of the MoSAIC model can be used to delineate the influence of each source of heterogeneity on the outcome. Given the marginal model from equation 2, we can write the joint covariance of our outcomes ($\hat{\Sigma}_Y$) as the summation of four matrices: $\hat{\Sigma}_Y = \hat{\Sigma}_X + \hat{\Sigma}_Z + \hat{\Sigma}_\psi + \hat{\Sigma}_\epsilon$. Thus, the variability in our outcome explained by the tumor gradient ($\hat{\Sigma}_X$), patient differences ($\hat{\Sigma}_Z$), the spatial relationship

between FOVs ($\widehat{\Sigma}_\psi$), and the measurement error ($\widehat{\Sigma}_\epsilon$). Analogous to R^2 in ANOVA and regression (Lynch 2013; Nakagawa & Schielzeth 2013), we can find the variance contribution attributable to each source of heterogeneity using the percentage of variance explained (PVE) as:

$$PVE[\Sigma_{(\cdot)}] = \frac{\text{trace}[\Sigma_{(\cdot)}]}{\text{trace}[\Sigma_Y]} \times 100.$$

We estimate the traces for Σ_X, Σ_Z , and Σ_ψ from the empirical variance of the MCMC samples of $B\widehat{\theta}, Z\widehat{\mu}$, and $\widehat{\psi}$, respectively. Σ_ϵ is estimated by $\bar{\sigma}_y^2 I_N$, where $\bar{\sigma}_y^2$ is the posterior mean of the measurement error. The PVE allows us to discern relative contribution of the tumor gradient in explaining changes in y compared to the between-patient heterogeneity and the spatial relationships between the FOVs.

3 Simulations

To demonstrate the effectiveness of MoSAIC, we conduct replicated simulation studies via ablation experiments to evaluate performance in terms of estimation accuracy, model fit, and prediction. We begin by outlining the HMI data generation process, followed by descriptions of the competing methods and comparative metrics. We assess the performance of MoSAIC under three scenarios: low spatial dependence (Scenario 1), high spatial dependence (Scenario 2) and non-linear tumor gradient effects (Scenario 3). All results are aggregated over 200 independent replicates

Simulation design. Across all scenarios, we generate 200 data sets with 300 FOVs distributed unequally among 20 patients such that $y = \mu + g(X) + \psi + \epsilon$. We set $\sigma_y^2 = 50$ and sample our patient-specific intercepts such that $\mu \sim N(50, 2\sigma_y^2 I_{20})$. In Scenarios 1 and 2, we assume a linear covariate effect ($g(X) = X\theta_1$) while in Scenario 3, we specify a non-linear effect, $g(X) = \arctan(X)_1$. In the low spatial dependence setting (Scenario 1), the measurement error σ_y^2 and the spatial variance τ^2 are equal, so that between-patient

differences account for more of the variability in the outcomes than the spatial structure. In Scenario 2, τ^2 is ten times larger than σ_y^2 , so now spatial dependence dominates outcome variability relative to between-patient differences. We also decrease the spatial decay parameter to reflect a weaker and stronger spatial coherence across FOVs in scenarios 1 and 2, respectively. Scenario 3 specifies a spatial dependence strength intermediate between those of Scenarios 1 and 2. We hypothesize that MoSAIC’s performance relative to currently applied models will improve as the spatial dependency between FOVs increases and in the presence of non-linear covariate effects.

Comparative metrics and methods. We assess estimation accuracy via mean squared error (MSE) of the covariate curves $g(\cdot)$ and model fit for through rescaled WAIC (Gelman et al. 2014). To evaluate predictive accuracy, 30 FOVs (10%) are withheld as a test dataset in each simulation, enabling calculation of the mean squared predictive error (MSPE) and the 95% predictive coverage of both y (details in Supplement Section S2). We compare these metrics across four models: MoSAIC, a non spatial version of MoSAIC without a spatial random effect, ψ , in equation 1 (Non-Spatial), a generalized additive model with random effects for patients (GAM; Hastie & Tibshirani 2014), and a spatial regression fit with a conditional autoregressive (CAR) spatial random effect (Spatial_CAR). We implement the Spatial_CAR model specified by Leroux et al. (1999) through the CARBayes package by Lee (2013). We use R package gam to implement the GAM model (Hastie 2025). We can recover samples of μ, θ, ψ by sampling from their posteriors to be used later for prediction (details in Supplement Section S2). We specify that ψ has a mean of 0 within a tumor tissue, $\frac{1}{n_i} \sum_{j=1}^{n_i} \psi(s_{j(i)}) = 0$ for all i , to improve identifiability between ψ and μ . For the non-linear simulation scenario, we use the R package mgcv (Wood 2017) to form the splines for MoSAIC and Non-Spatial models. We use the bs function by Bates & Venables (2025) for the Spatial_CAR model and smoothing splined with 5 degrees of freedom for the GAM. We use the rancmc package to update the proposal covariance (Helske 2021).

We run 60,000 MCMC iterations with an adaptive phase of 30,000 iterations and total burn-in of 45,000.

Results. Figure 2 summarizes the performance of each model across all three scenarios, where each box plot displays the distribution of each metric over the 200 simulated datasets, colored by model. Across all three simulation scenarios, MoSAIC achieves lower (better) WAIC, lower MSPE, and closer-to-nominal 95% predictive coverage than all competing models, with comparable or lower MSE. The left-most panel shows the distribution of WAIC values, with MoSAIC consistently achieving lower values, indicating a better model fit to the data. The center panel of Figure 2 shows how the MSE values of $g(X)$ across all 200 simulations, with lower values indicating improved estimation accuracy. The GAM model achieves the lowest MSE in the low spatial dependence setting. However, its performance declines as the spatial dependency and the covariate curve complexity increase. In Scenarios 1 and 2, MoSAIC has lower MSE than the Non-Spatial and Spatial_CAR models. In the non-linear setting, MoSAIC produces slightly higher MSE than the Non-Spatial model (15% higher), though the fitted curves are often visually comparable (Supplement Figure S1). The small losses in efficiency of MoSAIC are countered by the considerable gains in predictive accuracy, as shown by the distribution of MSPE in the right most box-plot. For example, MoSAIC has an MSPE that is 15%, 64%, and 60% lower than the Non-Spatial model in Scenarios 1, 2, and 3, respectively. Moreover, the average predictive coverage for MoSAIC is about 95% in the linear scenarios and increases from 95.3% for the point-wise credible bands to 99% for the joint credible bands in the non-linear scenario. Additional simulation details can be found in Supplement Table S1.

In summary, MoSAIC demonstrates consistently strong and often superior performance across varying degrees of spatial dependence and covariate function complexity relative to currently available methods applied to HMI data. The substantial gains in model fit

and predictive accuracy as spatial dependence increases confirm the importance of jointly modeling patient-level and spatial random effects in this data context, and support MoSAIC as a methodologically principled choice for the analysis of multi-resolution spatial data.

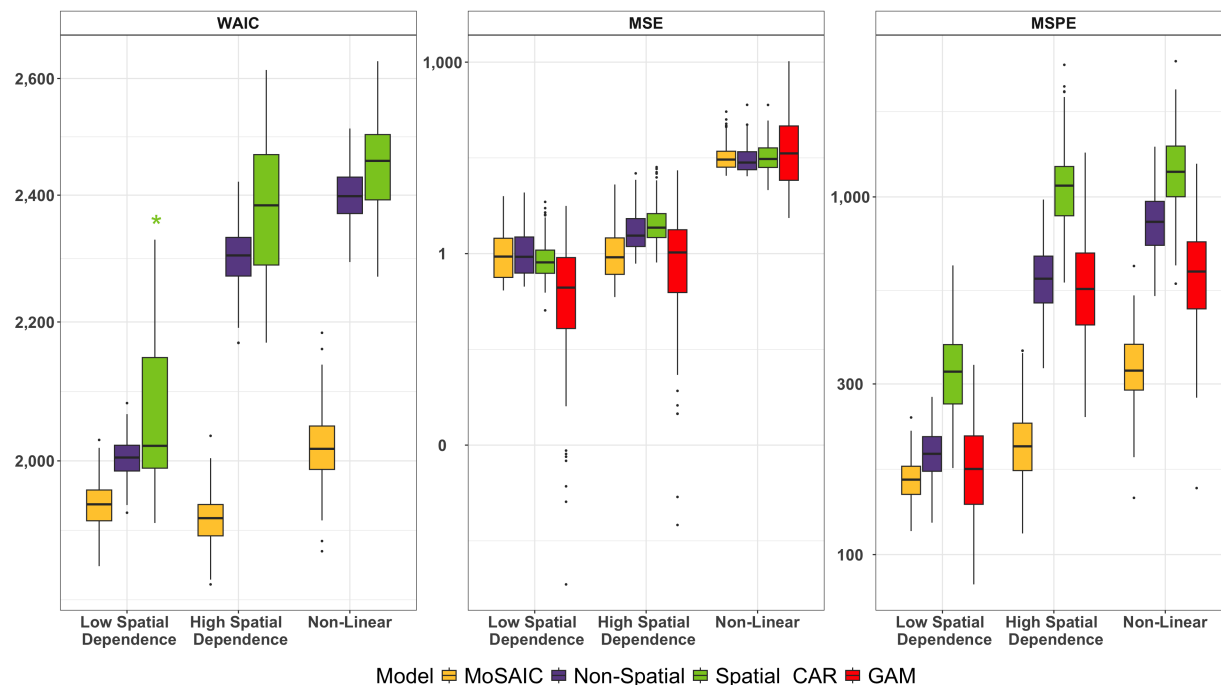


Figure 2: **Simulation performance of MoSAIC.** Each box plot is colored to indicate which of the four models it represents. The left panel plots the WAIC values for Bayesian models to assess model fit. The middle panel plots the MSE of $g(X)$ to assess estimation accuracy. The right panel plots the MSPE to assess models predictive accuracy. The y axis on the log base 10 scale. Three WAIC values for the Spatial_CAR model in Scenario 1 were less than 1,000 and removed for clarity as indicated by (*).

4 Spatial Tumor Gradients in Renal Cell Carcinoma

Our motivating RCC HMI dataset arises from a study of $N = 354$ FOVs across $I = 21$ patient tumor tissues with both clear cell RCC and sRCC features following established imaging protocols (McGue et al. 2023; May et al. 2025). Specifically, Vectra® Polaris™ Work Station and inForm® Cell Analysis™ software (Akoya Biosciences) were used to ob-

tain images and quantify marker expressions, respectively. The resulting quantification of 3 phenotypic markers (CD4, CD8, and CD163) defines 4 cell types: helper T, cytotoxic T, macrophages, and Tumor (see Supplemental Table S2). On average, tumor cells are the most abundant, comprising over 90% of the total cells within an FOV, while macrophages are the rarest occurring cell at 0.1% of total cells within an FOV. We quantify cellular colocalization using a distance-based metric DIMPLE by [Masotti et al. \(2023\)](#), y_{DIMPLE} , rescaled such that 0 indicates complete separation (no colocalization) and 100 indicates perfect spatial overlap (high colocalization) in each FOV (see Supplement Section S3). Figure 3 shows the distribution of y_{DIMPLE} for each pair of cells, demonstrating the variability in cell colocalizations across both FOVs and cell pairs. Two functional biomarker expressions

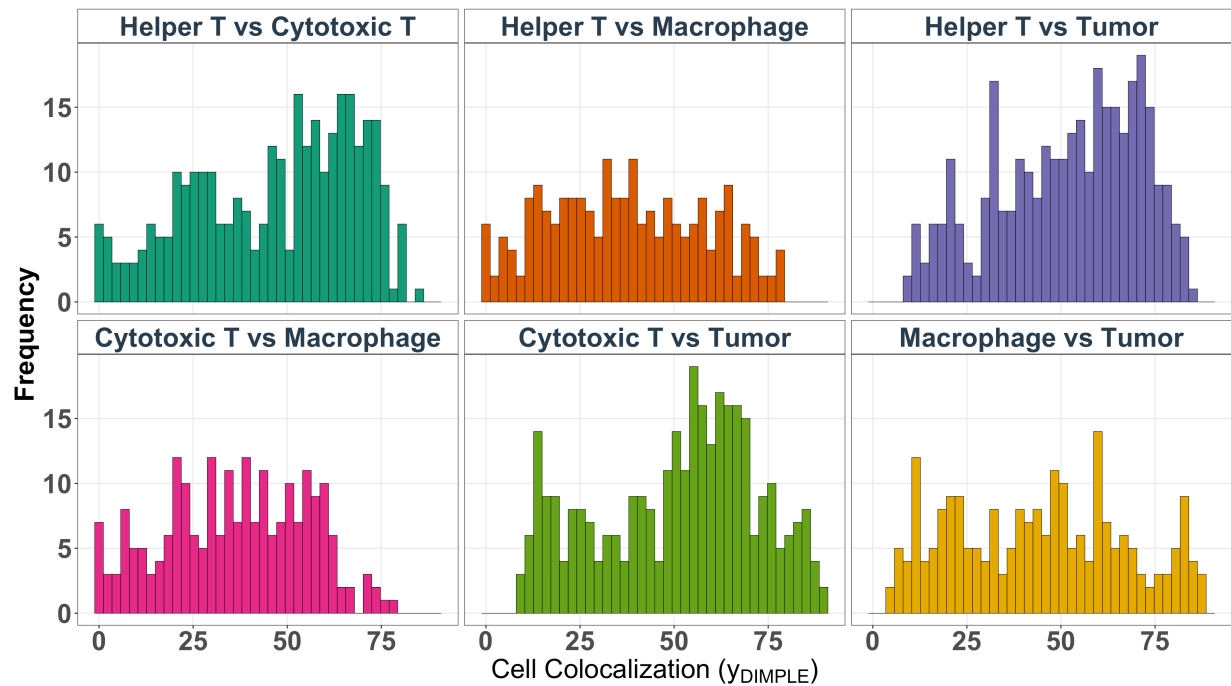


Figure 3: **Distribution of cell colocalization within FOVs across pairwise comparisons.** Each panel shows the distribution of cell colocalization scores across FOVs for each of the six pair of cells. The x-axis is the adjusted DIMPLE distance colocalization score and the y-axis is the number of FOVs with that colocalization score across all 21 patients.

define the tumor gradient at the FOV level: Programmed Death Ligand 1 (PD-L1) and N-cadherin (NCAD). PD-L1, which is a common target for cancer immunotherapies, has increased expression in sarcomatoid dedifferentiated tumors (Chandrasekaran et al. 2019) and NCAD is typically expressed at higher levels in more mesenchymal-like cells (Zeisberg & Neilson 2009). Thus, higher NCAD and PD-L1 expression indicates more advanced progression along the EMT gradient toward sRCC. Since our outcomes are measured at the FOV level, we summarize cellular NCAD and PD-L1 expression across FOVs (details in Supplement Section S3). Using MoSAIC, we investigate (a) the global, across patients relationships between cell colocalizations and the tumor gradients defined by PD-L1 and NCAD, and (b) how the spatial gradients between FOVs differ among the six cell-type pairs.

We implement 6 independent models, one for each pairwise cell colocalization, as follows:

$$y_{\text{DIMPLE}} = g(\{\mathbf{PD-L1}, \mathbf{NCAD}\}) + Z\mu + \psi + \epsilon. \quad (3)$$

We use penalized splines with 5 knots and a common shrinkage (σ_X^2) to capture the tumor gradient effect of PD-L1 and NCAD on the colocalization between a pair of cells. Each model includes FOVs with at least 1 of each cell type, with all models having a sample size between 215 and 325. We run MoSAIC for 60,000 MCMC iterations with a burn-in of 45,000, yielding 15,000 posterior samples in 4.4 to 9.7 minutes on a laptop with an M1 chip and 16GB of memory. We determine model convergence through trace plots of MCMC samples and by using Geweke diagnostic scores (Geweke 1992; see Supplement Figure S2 and Table S3). Our results are summarized as follows: global and patient specific PD-L1 and NCAD effects, the percentage of variance explained by each component in Equation 3, and the variability in spatial gradients across models.

PD-L1. The global associations between PD-L1 expression and the six pairwise cell colocalizations are shown in Figure 4A. Our results show two unique patterns of associations.

Most associations display an increasing pattern in colocalizations with PD-L1 expression initially, suggesting a potential increase in immune activity. As indicated by the orange lines on the x-axis, macrophages continue to co-locate significantly closer to all other cells as PD-L1 increases (middle row and bottom-right). The other three curves eventually return to 0 (top row and bottom-left). PD-L1's increasing relationship with macrophages and tumor cell colocalization (bottom-right) and the non-monotonic relationship with cytotoxic T cells and tumor cell colocalization (top left) may explain why sRCC has a worse prognosis and increased susceptible to immunotherapy overall. Increased PD-L1 expression is associated with increased tumor-associated macrophages, T cell inhibition, and worse prognosis (Tripathi et al. 2014). Thus, therapies that inhibit PD-L1 may improve T cell tumor infiltration and address this attenuated immune response to the tumor. Figure 4B shows patient specific curves, which highlights the noticeable between patient variability. Much of the limited data at higher PD-L1 expressions belonging to only two patients.

NCAD. Figure 5A shows the analogous global tumor gradient associations between NCAD expression and the six pairwise cell colocalizations. We see significant associations between cytotoxic and Tumor (top-right) and helper T vs cytotoxic T (bottom-left) colocalizations with NCAD (marked in orange on the x-axis). In both instances, lower values of NCAD indicate higher colocalization with a decreasing pattern as the expression of NCAD increases. This finding of increased cellular engagement between cytotoxic T cells and tumor cells at the lower end of the EMT gradient is consistent with previous findings (May et al. 2025) and suggests poorer immune targeting of tumor cells in sRCC tissue. Since cytotoxic T cells are primarily responsible for tumor cell destruction, less colocalization between cytotoxic T and tumor cells may suggest lower infiltration in higher EMT gradients (more mesenchymal regions). Moreover, May et al. (2025) found that visually, cytotoxic T cells tend to cluster near the boundary of sRCC, which may explain the change from initially higher to lower colocalization between these cells as NCAD increases. Figure

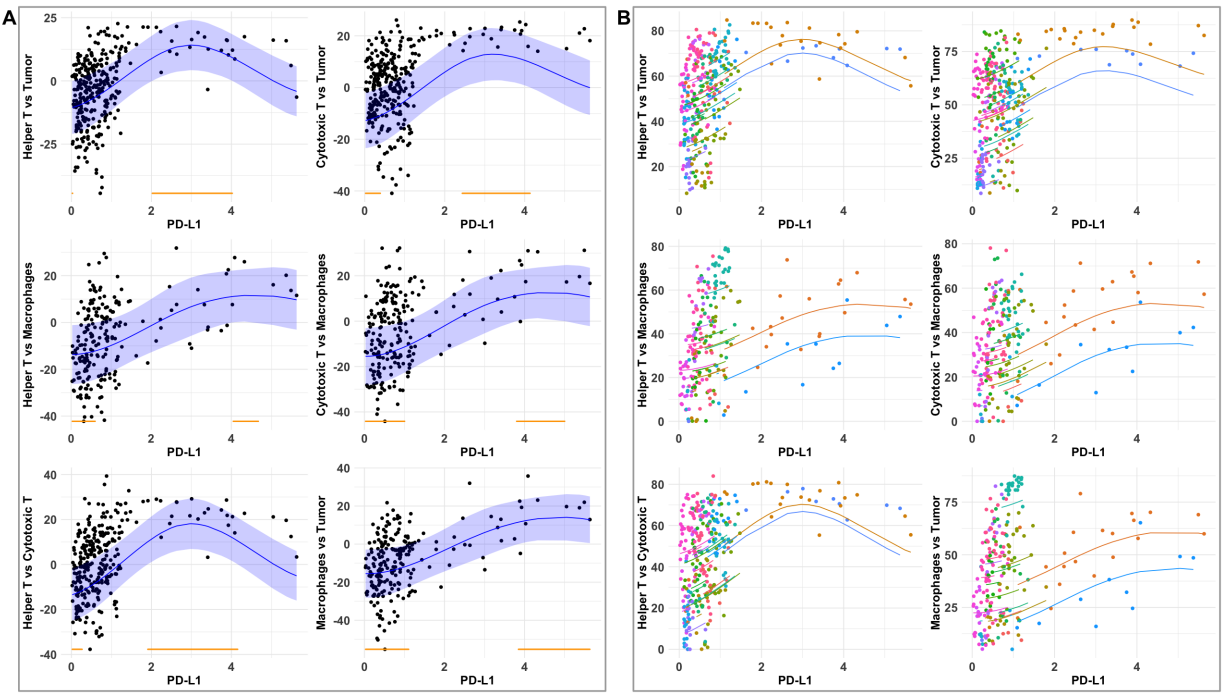


Figure 4: **A. Global curve for the associations between PD-L1 and pairwise cellular colocalizations with joint credible bands.** The y-axis is the cell colocalization centered at the patient intercept. Orange lines indicate locations where our curve significantly deviates from 0 and blue shaded ribbons display the joint credible bands. **B. Patient-specific curves for the association between PD-L1 and pairwise cellular colocalizations.** Each color and curve represents a unique patient ID.

5B shows the corresponding patient-specific curves and their deviations from global effects. Analogous to PD-L1, there is considerable inter-patient heterogeneity, primarily stemming from differing numbers of FOVs among the patients.

Percentage of Variance Explained and Spatial Gradients. Figure 6A shows the PVE across the 6 models from different sources, namely patient-specific, global covariate effects (PD-L1 and NCAD), spatial random effects, and measurement error. Overall, our MoSAIC model is able to explain at least 75% and up to 90% of the total variability in our outcomes with the rest attributed to measurement error. Congruent to Figures 4 and 5, the majority of the variance in our outcomes is captured by the patient-specific effects,

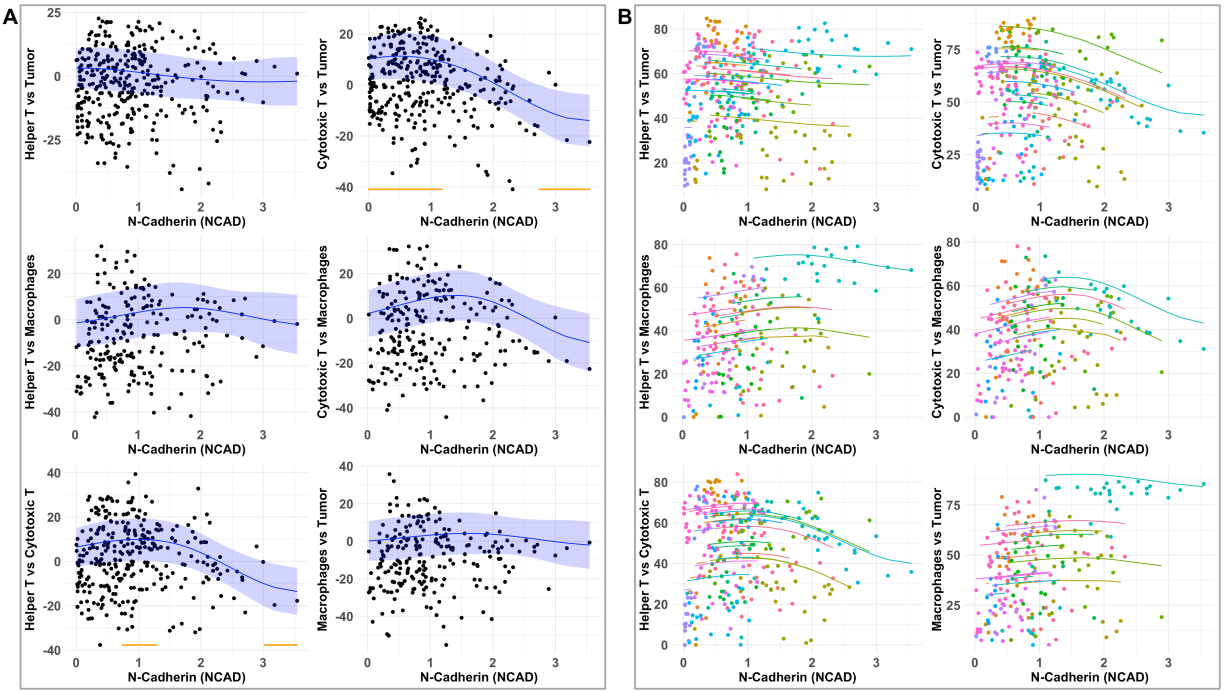


Figure 5: **A. Global curve for the associations between NCAD and pairwise cellular colocalizations.** The y-axis is the cell colocalization centered at the patient intercept. Orange lines indicate locations where our curve significantly deviates from 0 and blue shaded ribbons display the joint credible bands. **B. Patient-specific curves for the association between NCAD and pairwise cellular colocalizations.** Each color and curve represents a unique patient ID.

accounting for 29% to 54%, and PD-L1 accounts for more of the variance as compared to NCAD across all models (8%-13% vs <1%-5%). Finally, the percentage of spatial variability between FOVs varies across models, ranging from 11% to 30%, indicating the existence of non-negligible spatial variation accounted for by MoSAIC.

To further explore the spatial gradients, Figure 6B summarizes the spatial correlations across each of the six models. The curves show the decrease in spatial correlation of the cell colocalization measures between two FOVs as a function of their distance. Vertical lines indicate the average distance between first and second order FOV neighbors across the 21 tumor tissues, with high to moderate spatial gradients. The helper T-tumor cell

colocalizations had the most coordinated spatial gradient, with the correlation between FOVs decreasing slightly from 0.95 to 0.89 between first- and second-order FOV neighbors. The spatial gradient is less smooth for cytotoxic T-macrophage colocalization, with the correlation dropping from 0.69 to 0.40 between first- and second-order neighbors.

We further ran a goodness of fit test comparing the WAIC and DIC of MoSAIC to the non-spatial alternative presented in Supplement Table S4. MoSAIC fits the data better in each of the 6 models, further supporting the inclusion of spatial random effects between FOVs in our analysis.

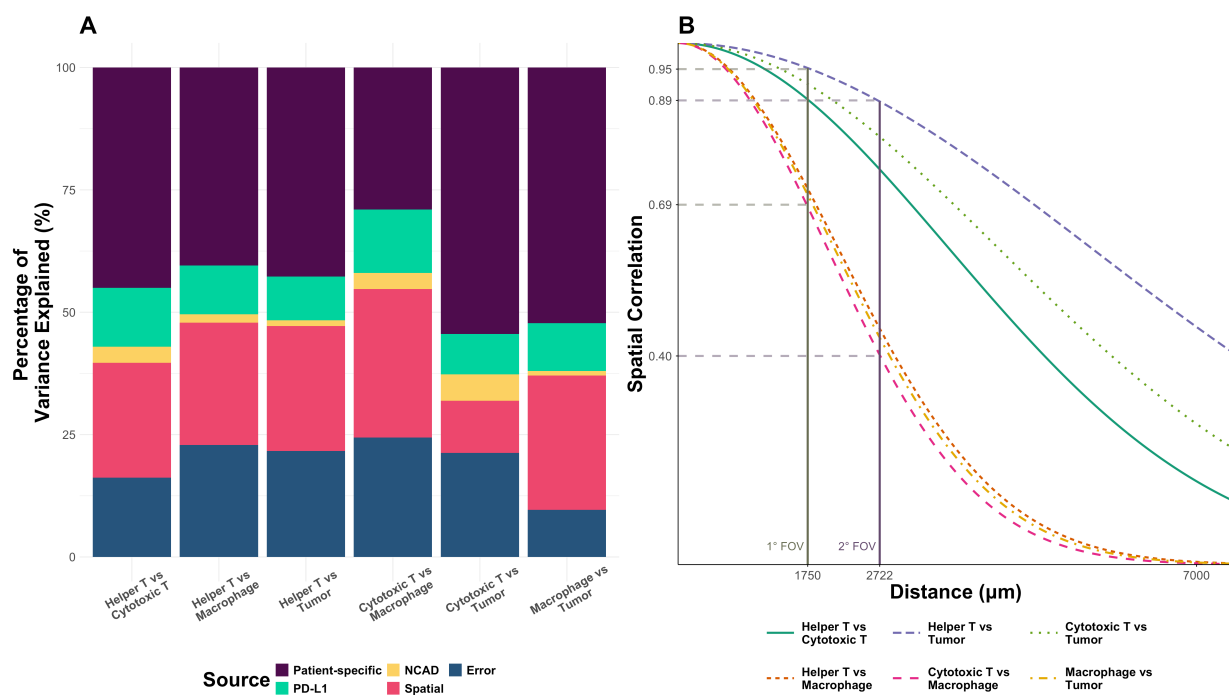


Figure 6: **A. The percentage of variance explained by each component of the MoSAIC regression model.** Each bar is a pairwise cell colocalization model. Each color represents the relative contribution of each a source of variability to the total variance. Top: patient-specific (purple)- PD-L1 (green)-NCAD(yellow)-spatial(red)-measurement error (blue):Bottom. **B. Spatial Gradients across the six pairwise cell-colocalization models.** Curves illustrate the spatial correlation between FOVs at a given distance. Vertical lines indicate the average distance between first- and second-order neighbors.

5 Discussion

We propose a novel hierarchical Bayesian spatial regression model, **MoSAIC**, for multi-resolution spatial imaging data, which complements current scientific understanding of spatial heterogeneity of TME in cancer. By explicitly delineating sources of variability and borrowing information across replicated spatial surfaces, **MoSAIC** reveals global biological trends, estimates tumor gradients, and characterizes their associations with the TME. Simulation studies demonstrate that **MoSAIC** achieves superior prediction accuracy and model fit relative to existing spatial and non-spatial alternatives, with performance gains most pronounced in settings with strong spatial dependence and complex tumor gradients.

Motivated by and applied to an sRCC HMI dataset, **MoSAIC** identifies that increased PD-L1 expression is associated with greater macrophage and tumor cell colocalization, consistent with the established literature linking elevated PD-L1 to an increase in tumor-associated macrophages. The initially increasing colocalization of T cells with tumor cells as PD-L1 expression rises may further indicate partial immune infiltration of sRCC that is functionally suppressed until PD-L1 is inhibited, offering a mechanistic basis for the heightened immunotherapy susceptibility observed in sRCC. Additionally, cytotoxic T cell–tumor cell colocalization decreases with increasing NCAD expression, suggesting lower immune targeting in more mesenchymal regions. This change in cell colocalization could explain the poorer prognosis of sRCC, suggesting a potentially reduced capacity of the immune system to target tumor cells in sRCC regions. Our model captures at least 75% of total variance in pairwise cellular colocalizations models, demonstrating strong explanatory power across multiple resolutions of heterogeneity. Generally, patient specific effects account for the largest PVE, though spatial relationships between FOVs accounting for 10% – 30%. This, in addition to the substantial improvement in fit over non-spatial models, underscores the importance of explicitly modeling spatial structure in HMI data and affirms **MoSAIC**'s

profitability in such settings. Beyond its inferential capabilities, **MoSAIC** is computationally efficient, with each model fit within minutes on a standard laptop (see Supplementary Table S1). In summary, **MoSAIC** offers a unified investigation of the TME across patients, incorporating several layers of heterogeneity originating from spatial dependence and between- and within-patient variability.

MoSAIC is broadly applicable to hierarchical or multi-resolution spatial imaging data for assessing tumor gradients across patient cohorts, and several natural extensions would further enhance its scope. Incorporating patient-level covariates, such as treatment response or cancer stage, would attribute additional variance to clinically relevant sources and incorporate yet another resolution. Currently, we model all pairwise cellular colocalizations independently, which allows us to investigate colocalizations with very different spatial gradients as shown in Figure 6B. Joint modeling of multiple pairwise cellular colocalizations would enable exploration of multi-cellular interactions. For example, one could characterize the interplay among T cells, macrophages, and tumor cells along the PD-L1 gradient. Finally, **MoSAIC** can be extended to model higher-resolution cellular level data; however, doing so requires nontrivial methodological development to accommodate the substantial increase in dimensionality, from hundreds of FOVs to millions of cells. Developing scalable methods for this setting is an important direction for future research.

As cancer medicine advances toward increasingly personalized approaches, there is a growing need for rigorous statistical frameworks capable of integrating the multi-scale, spatially structured data generated by modern imaging technologies. Multiplex imaging and related platforms provide an exceptionally rich source of biological information, but realizing their full scientific potential demands models that are both methodologically principled and scientifically motivated. **MoSAIC** addresses this need directly, filling a critical methodological gap by enabling quantitative, multi-resolution investigation of the spatial processes govern-

ing tumor biology. Its capacity to identify potential biomarker targets within the tumor gradient positions MoSAIC as a valuable tool for advancing immunotherapy development and, more broadly, for deepening our quantitative understanding of the microenvironmental drivers of patient outcomes.

6 Acknowledgments

JA's work was supported by the Rogel Cancer Center Graduate Student Scholarships of the University of Michigan Rogel Cancer Center and was partially supported by National Institutes of Health grant CA 83654. VB's work was supported by the National Institutes of Health grants R01CA244845-01A1 and P30 CA46592 and funds from the University of Michigan Rogel Cancer Center and School of Public Health. GPT 5.2 Generative AI model ([OpenAI 2025](#)) was used in accordance with journal guidelines to refine the grammar/tone of the paper, format BibTeX citations, and refine the elements of the latex displays (algorithms and tables). Claude Sonnet 4.6 ([Anthropic 2026](#)) and GPT 5.2 were used to annotate and streamline R scripts for public access on Github repository [jcaldous/MoSAIC](#). All outputs were reviewed and revised to display accurate information. These tools were accessed through the University of Michigan GenAI Services ([University of Michigan 2026](#)) and Visual Studio Codes' Github co-pilot extension ([GitHub 2026](#)).

7 Data Availability Statement

Data will be available with the publication of [May et al. \(2025\)](#), whose preprint can be found on bioRxiv. Multiplex immunofluorescent data will be shared by the lead contact, Dr. Evan Keller, upon request at etkeller@umich.edu.

References

- Anderson, N. M. & Simon, M. C. (2020), ‘The tumor microenvironment’, *Current Biology* **30**(16), R921–R925.
- Anthropic (2026), ‘Claude sonnet 4.6’. [Large language model].
URL: <https://www.anthropic.com/news/claude-sonnet-4-6>
- Arnol, D., Schapiro, D., Bodenmiller, B., Saez-Rodriguez, J. & Stegle, O. (2019), ‘Modeling cell-cell interactions from spatial molecular data with spatial variance component analysis’, *Cell Reports* **29**(1), 202–211.e6.
- Baddeley, A., Rubak, E. & Turner, R. (2016), *Spatial point patterns : methodology and applications with R*, Champan & Hall/CRC Interdisciplinary Statistics Series, CRC Press, Taylor & Francis Group, Boca Raton ;.
- Banerjee, S., Carlin, B. P. & Gelfand, A. E. (2015), *Hierarchical Modeling and Analysis for Spatial Data*, Chapman and Hall.
- Bates, D. M. & Venables, W. N. (2025), *Regression Spline Functions and Classes*, R Foundation for Statistical Computing. Version 4.5.0.
- Besag, J., York, J. & Mollié, A. (1991), ‘Bayesian image restoration, with two applications in spatial statistics’, *Annals of the Institute of Statistical Mathematics* **43**(1), 1–59.
- Blum, K. A., Gupta, S., Tickoo, S. K., Chan, T. A., Russo, P., Motzer, R. J., Karam, J. A. & Hakimi, A. A. (2020), ‘Sarcomatoid renal cell carcinoma: biology, natural history and management’, *Nature Reviews Urology* **17**(12), 659–678.
- Boyk, A., Wojas-Krawczyk, K., Krawczyk, P., Milanowski, J. & Tumor, J. (2022), ‘Microenvironment—a short review of cellular and interaction diversity’, *Biology* **11**, 929.

- Canete, N. P., Iyengar, S. S., Ormerod, J. T., Baharlou, H., Harman, A. N. & Patrick, E. (2022), ‘spicyr: spatial analysis of in situ cytometry data in r’, *Bioinformatics* **38**(11), 3099–3105.
- Chandrasekaran, D., Sundaram, S., Kadhiresan, N. & Padmavathi, R. (2019), ‘Programmed death ligand 1; an immunotarget for renal cell carcinoma’, *Asian Pacific Journal of Cancer Prevention* **42**, 2951–2957.
- Crainiceanu, C. M., Ruppert, D. & Wand, M. P. (2005), ‘Bayesian analysis for penalized spline regression using winbugs’, *Journal of Statistical Software* **14**(14), 1–24.
- De Boor, C. (1978), *A practical guide to splines*, Applied mathematical sciences (Springer-Verlag New York Inc.); 27, Springer-Verlag, New York.
- Dierckx, P. (1993), *Curve and Surface Fitting with Splines*, Clarendon Press / Oxford University Press, Oxford. Online edition, Oxford Academic, 31 Oct. 2023. Accessed 2 Nov. 2025.
- Eilers, P. H. C. & Marx, B. D. (1996), ‘Flexible smoothing with b-splines and penalties’, *Statistical Science* **11**, 89–121.
- Eliason, J. & Rao, A. (2024), ‘Investigating ecological interactions in the tumor microenvironment using joint species distribution models for point patterns’, *The New England Journal of Statistics in Data Science* **2**(3), 296–310.
- Eliason, J., Rao, A., Frankel, T. L. & Peruzzi, M. (2025), ‘Joint modeling of spatial dependencies across multiple subjects in multiplexed tissue imaging’. arXiv preprint.
- Gałecki, A. & Burzykowski, T. (2013), *Linear Mixed-Effects Model*, Springer New York, New York, NY, pp. 245–273.

- Gelman, A., Hwang, J. & Vehtari, A. (2014), ‘Understanding predictive information criteria for bayesian models’, *Statistics and Computing* **24**(6), 997–1016.
- Geweke, J. F. (1992), Evaluating the accuracy of sampling-based approaches to the calculation of posterior moments, *in* J. M. Bernardo, J. O. Berger, A. P. Dawid & A. F. M. Smith, eds, ‘Bayesian Statistics 4: Proceedings of the Fourth Valencia International Meeting, Dedicated to the Memory of Morris H. DeGroot, 1931–1989’, Clarendon Press, Oxford, UK, pp. 169–193.
- GitHub (2026), ‘Github copilot in vs code’.
- URL:** <https://github.com/features/copilot/ai-code-editor>
- Hastie, T. (2025), *gam: Generalized Additive Models*. R package version 1.22-7.
- Hastie, T. & Tibshirani, R. (2014), *Generalized Additive Models*, John Wiley & Sons, Ltd.
- He, H. & Magi-Galluzzi, C. (2014), ‘Epithelial-to-mesenchymal transition in renal neoplasms’, *Advances in Anatomic Pathology* **21**(3).
- Heidegger, I., Pircher, A. & Pichler, R. (2019), ‘Targeting the tumor microenvironment in renal cell cancer biology and therapy’, *Frontiers in Oncology* **14**(9).
- Helske, J. (2021), *ramcmc: Robust Adaptive Metropolis Algorithm*. R package version 0.1.2.
- Hinshaw, D. C. & Shevde, L. A. (2019), ‘The tumor microenvironment innately modulates cancer progression’, *Cancer research* **79**(18), 4557–4566.
- Huang, H. & Sun, Y. (2018), ‘Hierarchical low rank approximation of likelihoods for large spatial datasets’, *Journal of Computational and Graphical Statistics* **27**(1), 110–118.
- Kondo, A., Ma, S., Lee, M. Y., Ortiz, V., Traum, D., Schug, J., Wilkins, B., Terry, N. A., Lee, H. & Kaestner, K. H. (2021), ‘Highly multiplexed image analysis of intestinal tissue

- sections in patients with inflammatory bowel disease’, *Gastroenterology* **161**(6), 1940–1952.
- Lee, D. (2013), ‘CARBayes: An R package for Bayesian spatial modeling with conditional autoregressive priors’, *Journal of Statistical Software* **55**(13), 1–24.
- Lennon, J. (2000), ‘Red-shifts and red herrings in geographical ecology’, *Ecography* **23**, 101–113.
- Leroux, B. G., Lei, X. & Breslow, N. (1999), Estimation of disease rates in small areas: A new mixed model for spatial dependence, *in* M. E. Halloran & D. Berry, eds, ‘Statistical Models in Epidemiology, the Environment and Clinical Trials’, Springer-Verlag, New York, pp. 135–178.
- Lewis, S. M., Asselin-Labat, M.-L., Nguyen, Q., Berthelet, J., Tan, X., Wimmer, V. C., Merino, D., Rogers, K. L. & Naik, S. H. (2021), ‘Spatial omics and multiplexed imaging to explore cancer biology’, *Nature Methods* pp. 1–16.
- Lin, J., Izar, B., Wang, S., Yapp, C., Mei, S., Shah, P., Santagata, S. & Sorger, P. (2018), ‘Highly multiplexed immunofluorescence imaging of human tissues and tumors using t-cycif and conventional optical microscopes.’, *eLife* **11**(7).
- Lynch, S. M. (2013), *Comparing Means Across Multiple Groups: Analysis of Variance (ANOVA)*, Springer New York, New York, NY, pp. 117–126.
- Masotti, M., Osher, N., Eliason, J., Rao, A. & Baladandayuthapani, V. (2023), ‘Dimple: An R package to quantify, visualize, and model spatial cellular interactions from multiplex imaging with distance matrices’, *Patterns* **4**(12), 100879.
- May, A. M., Kadomoto, S., Williams, C., Soupir, A. C., The, S., McGue, J. J., Robinson, T., Shelley, G., Hayes, M. T., Fridley, B. L., Balasi, J. A., Ramos Echevarria, P. M., Dhillon, J., Nallandhighal, S., Acharyya, S., Chen, L., Aldous, J., Schurman, N., Bal-

- adandayuthapani, V., Frankel, T. L., Salami, S. S., Manley, B. J., Mehra, R., Udager, A. M. & Keller, E. T. (2025), ‘Spatial analysis reveals a novel inflammatory tumor transition state which promotes a macrophage-driven induction of sarcomatoid renal cell carcinoma’. bioRxiv preprint.
- McGue, J. J., Edwards, J. J., Griffith, B. D. & Frankel, T. L. (2023), Multiplex fluorescent immunohistochemistry for preservation of tumor microenvironment architecture and spatial relationship of cells in tumor tissues, *in* ‘Cancer Systems and Integrative Biology’, Springer, pp. 235–246.
- Meyer, M. J., Coull, B. A., Versace, F., Cinciripini, P. & Morris, J. S. (2015), ‘Bayesian function-on-function regression for multilevel functional data’, *Biometrics* **71**(3), 563–574.
- Mohammed, S., Masotti, M., Osher, N., Acharyya, S. & Baladandayuthapani, V. (2024), ‘Statistical analysis of quantitative cancer imaging data’, *Statistics and Data Science in Imaging* **1**(1), 2405348.
- Nakagawa, S. & Schielzeth, H. (2013), ‘A general and simple method for obtaining R^2 from generalized linear mixed-effects models’, *Methods in Ecology and Evolution* **4**(2), 133–142.
- OpenAI (2025), ‘Gpt-5.2’. [Large language model].
URL: <https://openai.com/index/introducing-gpt-5-2/>
- Panigrahi, N. (2020), Inverse distance weight, *in* B. Daya Sagar, Q. Cheng, J. McKinley & F. Agterberg, eds, ‘Encyclopedia of Mathematical Geosciences’, Springer International Publishing, Cham, pp. 1–7.
- Plummer, M., Best, N., Cowles, K. & Vines, K. (2006), ‘CODA: Convergence diagnosis and output analysis for mcmc’, *R News* **6**(1), 7–11.
- Ptacek, J., Locke, D., Finck, R., Cvijic, M.-E., Li, Z., Tarolli, J. G., Aksoy, M., Sigal, Y.,

- Zhang, Y., Newgren, M. & Finn, J. (2020), ‘Multiplexed ion beam imaging (MIBI) for characterization of the tumor microenvironment across tumor types’, *Laboratory Investigation* **100**(8), 1111–1123.
- Rasmussen, C. E. & Williams, C. K. I. (2005), *Gaussian Processes for Machine Learning*, MIT Press.
- Ripley, B. D. (1976), ‘The second-order analysis of stationary point processes’, *Journal of Applied Probability* **13**(2), 255–266.
- Ruppert, D., Wand, M. P. & Carroll, R. J. (2009), ‘Semiparametric regression during 2003–2007’, *Electronic Journal of Statistics* **3**, 1193–1256.
- Seal, S. & Ghosh, D. (2022), ‘MIAMI: mutual information-based analysis of multiplex imaging data’, *Bioinformatics* **38**(15), 3818–3826.
- Seal, S., Neelon, B., Angel, P. M., O’Quinn, E. C., Hill, E., Vu, T., Ghosh, D., Mehta, A. S., Wallace, K. & Alekseyenko, A. V. (2024), ‘Spaceanova: Spatial co-occurrence analysis of cell types in multiplex imaging data using point process and functional anova’, *Journal of Proteome Research* **23**(4), 1131–1143.
- Shaked, M. (1980), ‘On mixtures from exponential families.’, *Journal of the Royal Statistical Society: Series B (Statistical Methodology)* **42**(2), 192–198.
- Spiegelhalter, D. J., Best, N. G., Carlin, B. P. & Van Der Linde, A. (2002), ‘Bayesian measures of model complexity and fit’, *Journal of the Royal Statistical Society: Series B (Statistical Methodology)* **64**(4), 583–639.
- Tripathi, A., Drake, C. G. & Harshman, L. C. (2014), ‘Harnessing the PD-1 pathway in renal cell carcinoma: Current evidence and future directions’, *BioDrugs* **28**(6), 513–526.

University of Michigan (2026), ‘Generative ai at michigan’. Accessed: 2026-04-24.

URL: <https://genai.umich.edu/>

van Dam, S., Baars, M. J. D. & Vercoulen, Y. (2022), ‘Multiplex tissue imaging: Spatial revelations in the tumor microenvironment’, *Cancers* **14**(13), 3170.

Vihola, M. (2012), ‘Robust adaptive metropolis algorithm with coerced acceptance rate’, *Statistics and Computing* **22**(5), 997–1008.

Watanabe, S. & Opper, M. (2010), ‘Asymptotic equivalence of bayes cross validation and widely applicable information criterion in singular learning theory.’, *Journal of machine learning research* **11**(12).

Wood, S. N. (2017), *Generalized additive models: An Introduction with R*, 2 edn, Chapman and Hall/CRC.

Wrobel, J., Harris, C. & Vandekar, S. (2023), Statistical analysis of multiplex immunofluorescence and immunohistochemistry imaging data, *in* B. Fridley & X. Wang, eds, ‘Statistical Genomics’, Springer US, New York, NY, pp. 141–168.

Zeisberg, M. & Neilson, E. G. (2009), ‘Biomarkers for epithelial-mesenchymal transitions’, *The Journal of Clinical Investigation* **119**(6), 1429–1437.

Supplementary Materials for Multi-Resolution Spatial Regression Analysis of Cellular Colocalizations in Cancer Imaging

Table of Contents.

S1. Methods

S1.1. Estimating spatial decay ϕ

S1.2. Robust adaptive Metropolis-Hastings algorithm

S1.3. Joint credible bands and global significance

S2. Simulation

S2.1. Calculation of Predictive Coverage and Mean Squared Predictive Error

S2.2. Fitted covariate curves in the non-linear simulations

S2.3. Recovering β

S2.4. Summary Table for Simulation Results

S3. Sarcomatoid Renal Cell Carcinoma Analysis

S3.1. Tumor gradient and Immune Cell Definitions for Real Data Analysis

S3.2. Quantifying cell clustering within an FOV

S3.3. MoSAIC MCMC Convergence and Model Diagnostics

S1 Methods

S1.1 Estimating spatial decay ϕ

Before fitting MoSAIC, we estimate and fix the spatial decay hyperparameter ϕ . We implement a test and training procedure to select the best ϕ from a range of values ϕ_{range} as shown in Algorithm S1. For each potential value $\tilde{\phi}$, we fit an abbreviated model 1 with only the spatial random effects and measurement error to the residuals from the linear regression model, y^{resid} . Then, we use the posterior predicted mean for the withheld test data, y_{test}^{resid} , to calculate the root mean squared error. We fix the spatial decay at the value of $\tilde{\phi}$ with the lowest root mean squared error. The test-training function `phi_tt_parallel.R` includes an option to select the spatial decay using a log predictive score, which includes uncertainty calibration in the selection of ϕ , though we found that both criteria lead to similar selections (code at [jcaldous/MoSAIC](#)). For our real data analysis we considered spatial decay values from 0 to 15 in increments of 0.5.

S1.2 Robust adaptive Metropolis-Hastings algorithm

To improve convergence, we implement the robust adaptive Metropolis-Hastings procedure specified by [Vihola \(2012\)](#). Let γ be a vector of sampled parameters, and S is a lower triangular proposal variance update matrix. Given a target acceptance of 23.5%, each MCMC sample is derived following Algorithm S2. This update was implemented through the `ramcmc` function by [Helske \(2021\)](#) in R.

S1.3 Joint credible bands and global significance

For M MCMC samples, let $g^{(m)}(X)$ be a posterior sample from our estimated global curve for a given biomarker expression X within the domain of expression across all patients \mathcal{X} .

The $100(1-\alpha)^{th}$ joint-credible bands expand the equivalent point-wise credible bands such that the probability of $g(X)$ being in that interval is greater than or equal to $1-\alpha$ for *all values* of $X \in \mathcal{X}$. There are many intervals that satisfy this condition. We construct a $100(1-\alpha)^{th}$ joint credible band such that, for all values of $X \in \mathcal{X}$

$$I_\alpha(s) = \bar{g}(X) \pm q_{(1-\alpha)} \widehat{Std}\{\bar{g}(X)\} \quad (S1)$$

where $q_{(1-\alpha)}$ is the $(1-\alpha)$ quantile of $\mathcal{Z}^{(m)} = \max_{X \in \mathcal{X}} \left| \frac{g^{(m)}(X) - \bar{g}(X)}{\widehat{Std}[\bar{g}(X)]} \right|$.

An advantage of this joint credible band formulation is that by inverting Equation S1, we can derive Simultaneous Band Score probabilities, $P_{SimBaS}(X)$ which tests if the tumor gradient effect is significantly different from 0 ($g(X) = 0 \forall X \in \mathcal{X}$).

$$P_{SimBaS}(\mathbf{X}) = \frac{1}{M} \sum_{m=1}^M \left(\left| \frac{\bar{\mathbf{g}}(\mathbf{X})}{\widehat{Std}\{\bar{\mathbf{g}}(\mathbf{X})\}} \right| \leq \mathcal{Z}^{(m)} \right)$$

$$P_{\text{global}} = \min_{\mathbf{X}} \{P_{SimBaS}(\mathbf{X})\}$$

Algorithm S1 Procedure for estimating spatial decay ϕ

- 1: **Input:** $y, B, \mathcal{S}, M, \phi_{range}, \alpha_{test}$
 - 2: Compute OLS estimates $\hat{\beta}_{ols}$ for $y \sim B$ and residuals $y^{resid} = y - B\hat{\beta}_{ols}$
 - 3: Split data into training and testing sets with sizes $n_{train} = (1 - \alpha_{test}) \times N$ and $n_{test} = \alpha_{test} \times N$
 - 4: **for** $\tilde{\phi} \in \phi_{range}$ **do**
 - 5: Sample $\tilde{\gamma} = \{\tilde{\sigma}_y^2, \tilde{\tau}^2\}$ from a spatial-only robust adaptive Metropolis–Hastings algorithm with likelihood:
 - 6: $y_{train}^{resid} \sim N(0, \tilde{\sigma}_y^2 I_{n_{train}} + \tilde{\tau}^2 C_{\tilde{\phi}}(\mathcal{S}_{train}))$
 - 7: **for** $m = 1, \dots, M$ **do**
 - 8: $\Sigma^{(m)} = (\tilde{\sigma}_y^{2(m)} * I_N + \tilde{\tau}^{2(m)} C_{\tilde{\phi}}(\mathcal{S}))$
 - 9: Calculate the posterior predictive mean of y_{test}^{resid} given y_{train}^{resid} :
$$\mu_{test}^{resid,(m)} = \Sigma_{test,train}^{(m)} [\Sigma_{train,train}^{(m)}]^{-1} y_{train}^{resid}$$
 - 10: **end for**
 - 11: Average $\mu_{test}^{resid,(m)}$ over MCMC draws: $\bar{\mu}^{resid} = \frac{1}{M} \sum_{m=1}^M \mu_{test}^{resid,(m)}$
 - 12: Calculate the root mean squared error: $RMSE_{\tilde{\phi}} = \sqrt{\frac{1}{n_{test}} \sum_{i=1}^{n_{test}} (y_{test,i}^{resid} - \bar{\mu}_i^{resid})^2}$
 - 13: **end for**
 - 14: **Output:** $\phi_{best} = \operatorname{argmin}_{\tilde{\phi} \in \phi_{range}} (RMSE_{\tilde{\phi}})$
-

Algorithm S2 Adaptive Metropolis Update

Require: γ_{n-1} , S_{n-1} , target acceptance $\alpha_{\text{target}} = 0.235, n_{\text{adapt}}$

1: Draw $\mathbf{U}_n \sim \mathcal{N}(0, I)$

2: Compute proposal:

$$\mathbf{Z}_n \leftarrow \gamma_{n-1} + S_{n-1} \mathbf{U}_n$$

3: Compute acceptance probability:

$$\alpha_n \leftarrow \min \left(1, \frac{\pi(\mathbf{Z}_n)}{\pi(\gamma_{n-1})} \right)$$

4: $\gamma_n \leftarrow \begin{cases} \mathbf{Z}_n & \text{With probability } \alpha_n \\ \gamma_{n-1} & \text{otherwise} \end{cases}$

5: For $n \leq n_{\text{adapt}}$, update covariance factor S_n such that:

$$S_n S_n^T = S_{n-1} \left(I + n^{-2/3} (\alpha_n - \alpha_{\text{target}}) \frac{\mathbf{U}_n \mathbf{U}_n^T}{\|\mathbf{U}_n\|^2} \right) S_{n-1}^T$$

6: **return** γ_n, S_n

S2 Simulations

S2.1 Calculation of Predictive Coverage and Mean Squared Predictive Error

In simulation settings, we assessed the predictive performance of our models via the 95% predictive coverage and mean squared predictive error. First, we split the dataset into a training and testing set, withholding 30 observations for testing. We fit each model to the training data and used these MCMC samples to predict the outcomes of the test data y^{test} . We make model based predictions of our testing data for the MoSAIC and Non-Spatial models. For the Spatial_CAR model, we cannot make model based predictions of the spatial random effect at new locations. We use inverse distance weight interpolation for the CAR model in order to predict outcomes at new locations (Panigrahi 2020). The 95% predictive coverage and mean squared predictive error use the resulting predictions, $y^{*(m)}$, from Algorithm S3. The mean squared predictive error is defined as follows

$$MSPE = \frac{1}{n_{test} \times M} \sum_{m=1}^M \sum_{k=1}^{n_{test}} (y_k^{test} - y_k^{*(m)})^2.$$

Predictive coverage is the probability that the observed outcomes are captured by the estimated credible bands. The nominal coverage is 95%. Given M predicted outcomes for each test observation, $y_i^* = \{y_i^{*(1)}, \dots, y_i^{*(M)}\}$, we calculate the $100(1 - \alpha)\%$ predictive coverage ($\bar{PC}_{1-\alpha}$) as follows.

$$L_i, U_i \leftarrow \text{Quantiles}(y_i^*; \{\alpha/2\}, \{1 - \alpha/2\})$$

$$\bar{PC}_{1-\alpha} = \frac{1}{n_{test}} \sum_{i=1}^{n_{test}} (y_i^{test} \in [L_i, U_i]).$$

S2.2 Fitted covariate curves in the non-linear simulations

Figure S1 shows the fitted covariate curves for one of the simulation data sets in the non-linear scenario (Scenario 3). The gray dots are the observed data and the black line represents the true $g(X)$. Non-spatial model has slightly lower MSE than MoSAIC but visually the curves are very similar.

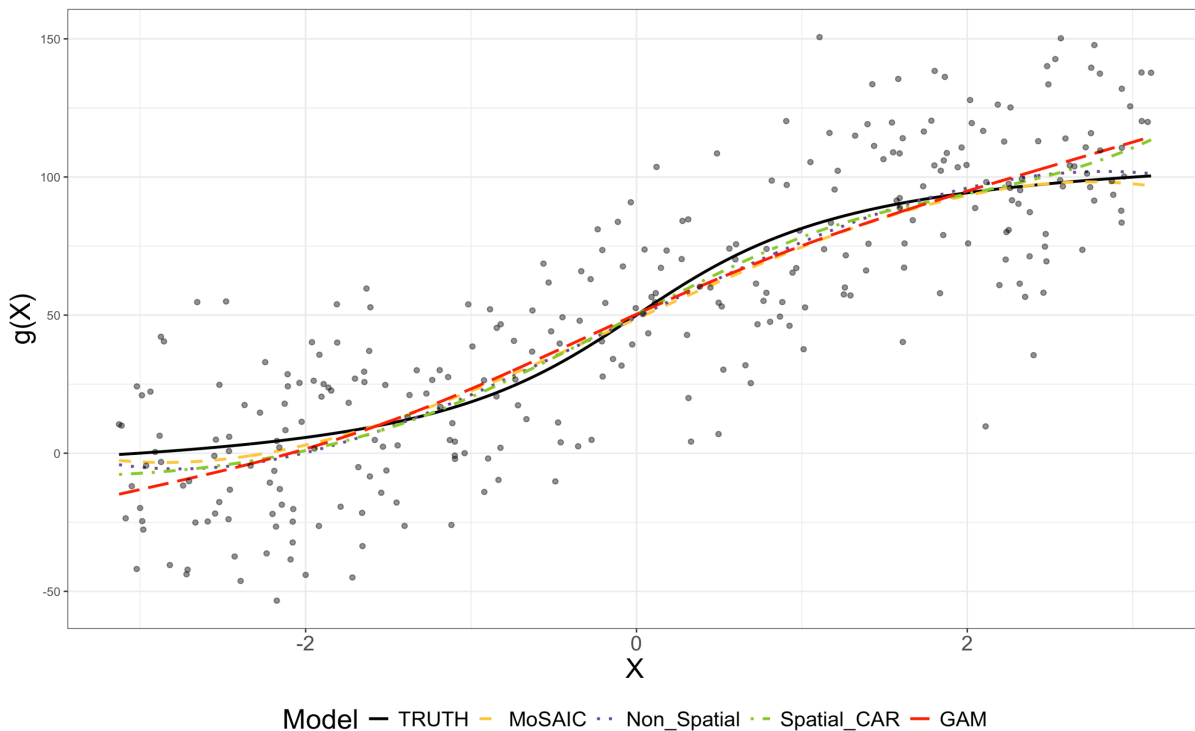


Figure S1: Plot of the true non-linear covariate effect (seed=5) and the estimated curve across all 4 models. The grey points are the observed data points and the black line represents the truth. While Non-Spatial has lower MSE than MoSAIC, their curves are very similar in shape

S2.3 Recovering β

Using samples of $\{\sigma_x^2, \sigma_y^2, \tau^2, \sigma_Z^2\}$, we jointly sample any patient-specific estimates (μ), biomarker estimates (θ), and latent spatial effects (ψ) from their posteriors. Thus, $\beta^T =$

$[\mu^T, \theta^T, \psi^T]$ is sampled from

$$p(\beta|y, Z, B, \tau^2, \sigma_x^2, \sigma_y^2, \sigma_Z^2) \sim N\left(V \begin{bmatrix} Z^T \Sigma_y^{-1} y \\ B^T \Sigma_y^{-1} y \\ \Sigma_y^{-1} y \end{bmatrix}, V\right)$$

$$V = \text{blockdiag} \left[\left(Z^T \Sigma_y^{-1} Z + \frac{1}{\sigma_Z^2} I_I \right)^{-1}, \left(B^T \Sigma_y^{-1} B + \sigma_x^{-2} K^{-1} \right)^{-1}, \left(\Sigma_y^{-1} + \frac{1}{\tau^2} C_\phi^{-1} \right)^{-1} \right].$$

S2.4 Summary Table for Simulation Results

The simulation results across three distinct data scenarios—Non-Linear, High Spatial Dependence, and Low Spatial Dependence—demonstrate the comparative performance of the MoSAIC model against Spatial (CAR), Non-Spatial, and GAM frameworks. Performance was evaluated using Watanabe-Akaike Information Criterion (WAIC), Mean Squared Error (MSE), Mean Squared Prediction Error (MSPE), 95% prediction coverage, and computation time. Table S1 includes the mean and standard deviations of WAIC, MSE, and MSPE under each simulation scenario. MoSAIC and Non-Spatial were the slowest overall but all models were fit in under 10 minutes when run on a laptop with M1 processor and 16GB of memory. R markdown tutorials for each simulation setting can be found in the Simulations folder at [jcaldous/MoSAIC](https://github.com/jcaldous/MoSAIC) on Github.

Table S1: Simulation Results Table

Characteristic	WAIC	MSE	MSPE	Prediction Coverage(95%)	Time to Fit
Non-Linear					
MoSAIC	2020 (47.9)	36.2(21.4)	342(74.9)	0.95 (0.04)	6 min
Spatial (CAR)	2456 (73.8)	38.2 (25.7)	1216(295)	0.91 (0.07)	8 sec
Non-Spatial	2400 (41.7)	33.3 (20.9)	864 (17)	0.94 (0.05)	4 min
GAM	-	77.4 (108)	629 (188)	0.95 (0.04)	<1 sec
High Spatial Dependence					
MoSAIC	1921 (33.3)	1.40 (1.51)	209 (50.6)	0.95 (0.05)	6 min
Spatial (CAR)	2379 (107)	3.60 (3.35)	1090 (276)	0.86 (0.11)	8 sec
Non-Spatial	2300 (47.2)	3.01 (2.74)	599 (120)	0.95 (0.04)	4 min
GAM	-	2.28 (3.45)	577 (192)	0.95 (0.04)	<1 sec
Low Spatial Dependence					
MoSAIC	1940 (31.7)	1.33 (1.27)	163 (22.4)	0.95 (0.04)	6 min
Spatial (CAR)	2045 (198)	1.03 (0.93)	335 (90.4)	0.87 (0.10)	8 sec
Non-Spatial	2002 (27.2)	1.46 (1.39)	193 (28.8)	0.95 (0.04)	4 min
GAM	-	0.68 (0.96)	181 (55.1)	0.95 (0.04)	<1 sec

[†]Mean (SD)

Algorithm S3 Predicting Outcomes Y^* for (MoSAIC and Spatial_CAR)

1: Model $\in \{\text{MoSAIC}, \text{Spatial_CAR}\}$, $X_{\text{test}}, y^{\text{test}}, M, \mathcal{S}, \mathbf{ID} = [\mathbf{ID}^{\text{train}}, \mathbf{ID}^{\text{test}}], \gamma_{\text{model}}$.

2: **for** $m = 1 \dots M$ **do**

3: **if** MoSAIC **then** $\gamma_{\text{model}}^{(m)} = (\theta^{(m)}, rI_{\text{train}}^{(m)}, w^{(m)}, \sigma_y^{2(m)}, \tau^{2(m)}, \sigma_{RI}^{2(m)})$

4: $C_\phi(\mathcal{S}) = \begin{bmatrix} C_{\text{train}} & C_{\text{test,train}}^T \\ C_{\text{test,train}} & C_{\text{test}} \end{bmatrix}$.

5: $\mu_{\text{fixed}}^{(m)} \leftarrow X_{\text{test}} \theta^{(m)}$

6: **for** $i = 1, \dots, n_{\text{test}}$ **do**

7: **if** $\text{ID}_i^{\text{test}} \in \mathbf{ID}^{\text{train}}$ **then**

8: $rI_i^{(m)} \leftarrow rI_{\text{train},j}^{(m)}$ with j such that $\text{ID}_i^{\text{test}} = \text{ID}_j^{\text{train}}$

9: **else**

10: $rI_i^{(m)} \leftarrow \mathcal{N}\left(0, (\sigma_{RI}^{(m)})^2\right)$

11: **end if**

12: **end for**

13: $w^{*(m)} \leftarrow \mathcal{N}\left(C_{\text{test,train}} C_{\text{train}}^{-1} w^{(m)}, \tau^{2(m)} (C_{\text{test}} - C_{\text{test,train}} C_{\text{train}}^{-1} C_{\text{test,train}}^T)\right)$

14: $\mu_{\text{pred}}^{(m)} \leftarrow \mu_{\text{fixed}}^{(m)} + rI^{(m)} + w^{*(m)}; V_{\text{pred}}^{(m)} \leftarrow \sigma_y^{2(m)}$

15: **end if**

16: **if** Spatial_CAR **then** $\gamma_{\text{model}}^{(m)} = (\theta^{(m)}, \phi_{\text{train}}^{(m)}, \sigma_y^{2(m)}, \tau^{2(m)})$, Distance Matrix D .

17: $\mu_{\text{fixed}}^{(m)} \leftarrow X_{\text{test}} \theta^{(m)}$

18: **for** $i = 1, \dots, n_{\text{test}}$ **do**

19: $w_{ij} \leftarrow (D_{ij} + \epsilon)^{-2}; \phi_i^{*(m)} \leftarrow \frac{\sum_j w_{ij} \phi_j^{(m)}}{\sum_j w_{ij}}$

20: **end for**

21: $\mu_{\text{pred}}^{(m)} \leftarrow X_{\text{test}} \theta^{(m)} + \phi^{*(m)}; V_{\text{pred}}^{(m)} \leftarrow \sigma_y^{2(m)} + \tau^{2(m)}$

22: **end if**

23: $y^{*(m)} \leftarrow \mathcal{N}(\mu_{\text{pred}}^{(m)}, V_{\text{pred}}^{(m)} I_{n_{\text{test}}})$

24: **end for**

25: **Output Predictions:** $Y^* = \{y^{*(1)}, \dots, y^{*(m)}, \dots, y^{*(M)}\}$

S3 Sarcomatoid Renal Cell Carcinoma Analysis

S3.1 Tumor gradient and Immune Cell Definitions for Real Data Analysis

The expression of PD-L1 and NCAD are measured across pixels of the cell and summarized into 5 distinct values: minimum, maximum, mean, total, and standard deviation. NCAD expression at the FOV level was defined as the average of mean cellular NCAD expression. Since PD-L1 expression is generally very low as seen in Figure 4, we defined FOV level PD-L1 expression as the sum of the total cellular PD-L1 across all cells within an FOV. The FOV level PD-L1 expression is rescaled to similar to NCAD expression by dividing by 1000. Table S2 outlines the immunophenotyping criteria for cells. These cellular phenotypes were used to define the pairwise cell colocalizations.

Table S2: Cell type definitions.

Cell type	Markers
Helper T	CD3+ and CD8- and CD163-
Cytotoxic T	CD8+ and CD163-
Macrophage	CD163+
Tumor	All remaining cells

S3.2 Quantifying cell clustering within an FOV

For our real data analysis, we used DIMPLE software to measure each pairwise cellular co-localization(Masotti et al. 2023). DIMPLE first generates a cell intensity function for each cell type and then calculates the pairwise distance between two cell intensities. The

Jensen-Shannon distance is an ideal choice for our setting because it is scientifically easy to interpret and is not sensitive to image artifacts (i.e. holes or tears). The Jensen-Shannon distance makes modeling cell co-occurrence more interpretable since we know a value of 0 indicates perfect overlap and 1 complete separation. We rescale the distance such that for a given dimple distance d_{dimple} ,

$$y_{dimple} = 100 * (1 - d_{dimple}).$$

Additionally, DIMPLE software requires no permutations and produces output ready for downstream modeling, making it efficient and well suited for our modeling needs. DIMPLE requires users to specify the grid size and smoothing distance in order to generate the initial cell-type intensities. In all our modeling, the grid is set to roughly the size of a cell (5 to 10 μm) and the smoothing is set to be between 20-60 μm , which is considered the sphere of influence of a cell (Masotti et al. 2023).

S3.3 MoSAIC MCMC Convergence and Model Diagnostics

Convergence of our models is assessed visually through the MCMC plots of the variance terms, which show our model is exploring the posterior well (Figure S2). Table S3 includes additional information about the MCMC samples of the variance terms. For each model, we report the posterior means and point-wise confidence intervals, the effective sample size(n effective) out of 15,000 and the Geweke Score. Absolute Geweke scores below 1.96 indicate no strong evidence against convergence. An n effective lower than 15,000 indicates larger autocorrelation between our samples. The n effective and Geweke scores are derived via the respective function in the coda R package (Plummer et al. 2006).

Table S4 compares the model fit of MoSAIC and the non spatial alternative via DIC and WAIC. The lower scores across all 6 models show the spatial MoSAIC model consistently fit the data better than when the spatial effect was omitted.

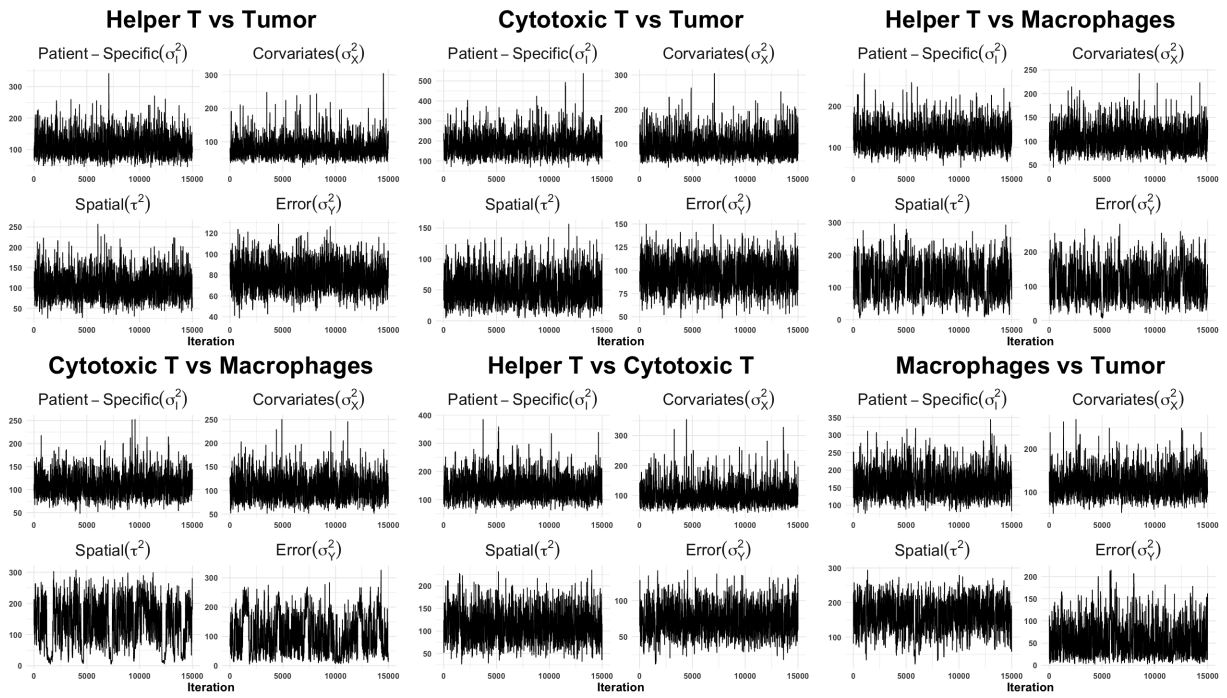


Figure S2: Traceplots for pairwise colocalization models

Table S3: Posterior Means and Credible intervals for MoSAIC models applied to RCC data

Model	Metric	σ_Y^2	τ^2	σ_I^2	σ_x^2
Helper T vs Tumor	Posterior Mean	77.7	103.1	110.8	78.7
	(CI)	(55.9, 102.8)	(54.2, 169.1)	(63.3, 187.5)	(43.7, 142.4)
	N effective	1042.6	1021.8	1066.2	974.1
	Geweke	0.40	-0.20	1.80	-1.80
Helper T vs Macrophage	Posterior Mean	107.0	119.3	124.0	104.0
	(CI)	(27.1, 213.4)	(19.4, 219.7)	(82.2, 186.6)	(66.8, 158.9)
	N effective	393.6	339.5	1023.7	1021.8
	Geweke	1.40	-0.80	1.10	0.00
Helper T vs Cytotoxic	Posterior Mean	71.4	110.3	138.7	101.8
	(CI)	(35.0, 111.2)	(53.3, 181.1)	(79.9, 223.7)	(57.4, 186.2)
	N effective	921.4	919.7	1034.5	876.8
	Geweke	-1.00	1.90	-1.30	0.20
Cytotoxic vs Macrophage	Posterior Mean	104.1	133.5	108.8	104.2
	(CI)	(15.2, 232.9)	(13.4, 248.7)	(71.4, 163.5)	(67.1, 159.1)
	N effective	163.2	157.7	899.7	1042.2
	Geweke	0.80	-0.70	0.20	0.10
Cytotoxic vs Tumor	Posterior Mean	93.6	50.5	176.9	93.2
	(CI)	(65.8, 124.1)	(13.8, 98.6)	(102.5, 289.1)	(51.9, 165.1)
	N effective	991.8	1038.9	992.2	1043.9
	Geweke	0.30	0.10	-1.20	0.80
Macrophage vs Tumor	Posterior Mean	55.1	159.3	160.1	116.3
	(CI)	(8.5, 145.3)	(60.9, 233.5)	(101.4, 243.2)	(74.1, 182.1)
	N effective	479.3	444.4	962.5	1059.8
	Geweke	0.60	-0.00	-0.50	-1.30

Table S4: Model fit metrics for MoSAIC vs Non-Spatial alternative in real data setting

Pairwise Cellular Colocalization	Model	DIC	WAIC
Helper T vs Tumor	MoSAIC	2454	2459
	Non-Spatial	2544	2543
Cytotoxic T vs Tumor	MoSAIC	2463	2472
	Non-Spatial	2498	2500
Helper T vs Macrophages	MoSAIC	1681	1710
	Non-Spatial	1787	1788
Cytotoxic T vs Macrophages	MoSAIC	1671	1738
	Non-Spatial	1838	1839
Helper T vs Cytotoxic T	MoSAIC	2311	2323
	Non-Spatial	2433	2435
Macrophages vs Tumor	MoSAIC	1581	1633
	Non-Spatial	1835	1835